(Received 11 July 2024, Accepted 6 September 2024, Scheduled 17 September 2024)

A Dual-Band MIMO Antenna Based on Multimode for 5G Smartphone Applications

Han Lin[1], Wenjie Sun[1,*], Zhonggen Wang[1], and Wenyan Nie[2]

[1]School of Electrical and Information Engineering, Anhui University of Science and Technology, Huainan 232001, China
[2]School of Mechanical and Electrical Engineering, Huainan Normal University, Huainan 232001, China

ABSTRACT: In order to meet the current demand for 5G smartphone antennas, this paper introduces a six-port dual-band multiple-input multiple-output (MIMO) antenna designed for 5G smartphones. Based on multimode, the antenna achieves multiple band coverage in a limited space, making it of significant practical value in 5G cell phone antenna applications. The antenna features a structure comprising a modified L-shaped patch antenna, a gun-shaped slot in the ground plane, and two small stubs extending from the metal ground. This configuration creates a multimode antenna that is excited by two coupled feed loop modes and two slot modes. The feeder strips, which have been enhanced with L-shaped slots, form tuned branches, enabling the co-excitation of multiple modes. The MIMO system can operate within the frequency range of 3.3–3.8 GHz and 4.4–7.5 GHz ($S_{11} < -6$ dB), covering the 5G communication bands including n78 (3.3–3.8 GHz)/n79 (4.4–5.0 GHz) and the LTE Band 46 (5.15–5.925 GHz). Additionally, the antenna exhibits an envelope correlation coefficient of less than 0.18, antenna efficiency ranging from 60% to 93%, and isolation between adjacent antenna elements better than 12.9 dB.

1. INTRODUCTION

5G has revolutionized data transmission rates, latency, mass connectivity, network reliability, and energy efficiency compared to its predecessors. The emphasis has been placed on the development of communication technologies for 5G terminals [1]. Multiple-input multiple-output (MIMO) system technology is an advanced method to meet the demand for high data rates because it transmits and receives signals through multiple antennas, realizing the improvement of channel capacity and spectral efficiency [2]. Since the realization of MIMO technology requires multiple antenna elements to be configured on the mobile device, this can be limited by the size of the antenna and the space of the mobile device, which affects the bandwidth and element isolation of the MIMO antenna and leads to a decrease in the transmission rate, reducing the effectiveness of the MIMO antenna. Therefore, the design of the MIMO antenna that maintains wide bandwidth and good isolation within the limited space of mobile devices is gaining more attention.

Different countries are focusing on various spectrums for deploying 5G communication bands. For instance, the U.S. has adopted 3.55–3.7 GHz and 3.7–4.2 GHz as the future 5G communication bands, while China has opted for 3.3–3.6 GHz and 4.8–5 GHz. Moreover, the frequency bands ranging from 5170 to 5835 MHz have been designated as the spectrum for 5G wireless local area network (WLAN). Currently, numerous studies are being conducted on antennas for 5G smartphone terminals, aiming to accommodate various frequency bands. Among them, MIMO antennas are being developed to support a single LTE band 42 (3.4–3.6 GHz) [3–14]. However, the bandwidth provided by these antennas is too narrow to meet the increasing demand for practical applications. Consequently, multiband antennas are being further explored to address the requirements of practical applications [15–22] and achieving excellent isolation levels exceeding 10 dB. In these designs, monopole, slot, loop mode, and inverted F antenna (IFA) are commonly utilized to generate multiple resonances. In [17], an antenna consists of four dual antenna arrays (DAA), each including a two-branch monopole antenna and a T-shaped decoupling stub. This antenna covers the n77 band (3.3–4.2 GHz) and 5 GHz band (4.8–5.0 GHz). The antenna proposed in [20] utilizes a combination of monopole and slot patterns and a high-pass low-rejection filter in the slot slit to achieve dual-band operation at 3.4–3.6 GHz and 4.8–5.0 GHz. Nevertheless, these designs typically function within bandwidths of 3.4–3.6 GHz and 4.8–5 GHz. This limited spectrum remains insufficient for future 5G communication deployments, and there is an ongoing expectation for bandwidth expansion.

Recently, several new and promising antenna array structures have been proposed, and the bandwidth has been further expanded to increasingly meet the needs of 5G communications [23–30]. In [23], each antenna unit is a slot antenna, which consists of an L-shaped slot and a 50 Ω microstrip feedline, and a 10 dB impedance broadband coverage of the 5G NR band and WLAN 5 GHz band can be realized by loading a tuning stub on the feedline. Ref. [24] proposes a dual-band 8-port MIMO 5G smartphone antenna with two open-slot metal frames and coupled feeds, enabling coverage of the n78 and n79 as well as WIFI 5 GHz bands and excellent isolation of 16.5 dB. In [25], a small low-profile ultra-wideband MIMO antenna designed to

* Corresponding author: Wenjie Sun (2023200721@aust.edu.cn).

contain vertical, horizontal strip lines and diagonal strip line cross-sections is proposed such that its resonance can cover the frequency range from 3.20 GHz to 13.40 GHz, and isolation is greater than 20 dB. The antenna in [28] consists of a monopole structure, an inverted L-pivot, and an inverted C-pivot, which allows the antenna to obtain multiple modes and improves impedance matching by utilizing parasitic elements, open slits, and stubs. The antenna's −6 dB impedance bandwidth fully covers the 5G sub-6 GHz NR bands n77/n78/n79. The single element of the antenna proposed in [29] consists of both open and closed slots, based on the simultaneous excitation of multiple slot patterns acting together to cover a broadband of 3.4–6.1 GHz, with isolation also reaching 11.7. In [30], three resonant modes (loop mode, slot mode, and PIFA mode) are well excited by etching a T-slot on the PIFA element. The three modes work together to achieve an ultra-bandwidth of 3.3–7.5 GHz, but their isolation is hardly more than 10 dB even with reduced mutual coupling through grounding piles. Also, the use of new materials has led to improved antenna performance. In [31], a superconducting flexible antenna that can be used for wearable electronic devices printed using a tri-nanocomposite of graphene nanosheets/silver/copper (GNP/Ag/Cu) is proposed, such that the material allows to obtain a high gain without reducing the safety.

In view of the above discussion and in order to overcome the drawbacks of narrow bandwidth and low isolation present in the above literature, this paper innovatively proposes the configuration of a six-port dual-band MIMO array using loop and slot modes. In terms of material selection, copper was chosen as the antenna conductive material, which is still able to have a better effect under the condition of not using new conductive materials. In design, the antenna array incorporates two low-frequency loop modes at approximately 3.5 GHz and 5.1 GHz, as well as two slot modes at around 5.8 GHz and 7.1 GHz, positioned along the perimeter of a gun-shaped slot. In terms of band selection, the antenna covers the mainstream 5G frequencies (n78 and n79) and LTE band 46. Such a choice of frequencies makes it possible to cope with the configuration of antennas for 5G smartphones. With such frequency selection, it can be configured for most of the 5G smartphone terminal antennas. Therefore, the antenna has research value and is suitable for 5G smartphones. To enhance impedance matching, the feeder structure was adjusted by adding tuned branches. The −6 dB impedance bandwidths of the four resonances are combined to cover a frequency range of 3.3–3.8 GHz and a wideband range of 4.4–7.5 GHz. Both simulated and measured outcomes demonstrate an isolation exceeding 12.9 dB and an envelope correlation coefficient (ECC) below 0.18.

2. ANTENNA DESIGN

2.1. Antenna Construction

Figure 1 illustrates the proposed six-port MIMO array configuration consisting of six antenna elements, labeled ANT1 through ANT6, with a centrally symmetric antenna arrangement mounted on the frame along the two longer sides. An FR-4 substrate (relative permittivity of 4.4, loss tangent of 0.02)

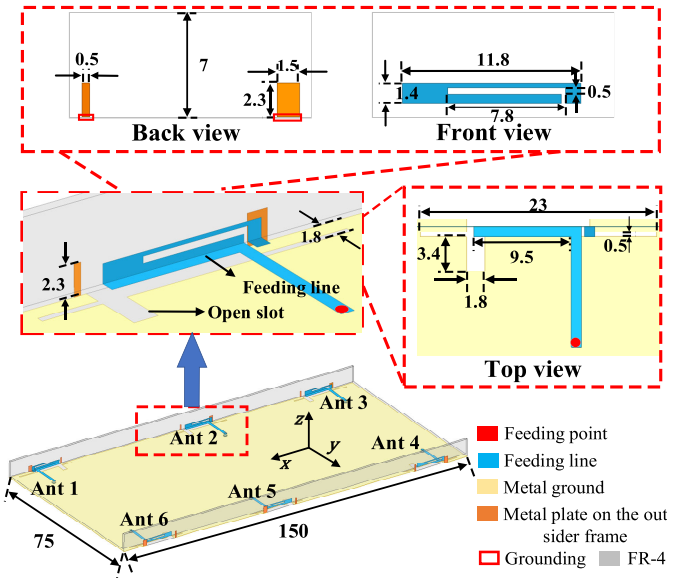

FIGURE 1. Construction and detailed dimensions of the MIMO array and single element (Unit: mm).

is used to simulate the frames with the main board of the system, with metal ground etched on the top and bottom sides of the substrate and on both sides of the frames. The dimensions of the motherboard are $150 \times 75 \times 0.8\,\text{mm}^3$, and the length of the frame is 75 mm, with a height of 7 mm and a thickness of 0.8 mm.

As illustrated in Figure 1, each individual antenna element comprises three distinct components: an L-shaped 50 Ω microstrip feeding line that has undergone modifications and advancements, a gun-shaped slot within the metal ground plane, and two minor metal patches situated on the external surface of the structure. The microstrip feed line consists of two parts joined together on the upper surface of the substrate and the inner surface of the frame. Below the microstrip line, a gun-shaped slot is etched into the metal ground plane beneath the substrate. Two small metal pieces etched on the outer surface of the frame act as upward extensions of the ground plane, connected to enhance the impedance-matching effect of the antenna elements. Each antenna element is fed by a folded 50 Ω microstrip feeding strip coupled with a Super Miniature A version (SMA) connector.

2.2. Antenna Evolution and Analysis

The evolution of the antenna design is depicted in Figure 2 while Figure 3 displays the reflection coefficients for the various schemes mentioned.

In [1], Figure 2(a) shows an L-shaped feedline, which is a simple etch on the upper surface of the substrate. However, it does not create an effective impedance match with the T-shaped slot in the ground. In [2], two small rectangular patches are introduced from the floor towards the outside of the frame to achieve good impedance matching. Additionally, the microstrip feedline is extended over the inner surface of the frame, as illustrated in Figure 3. Ref. [2] achieves good resonance in the high-frequency range. As illustrated in Figure 2(c) to

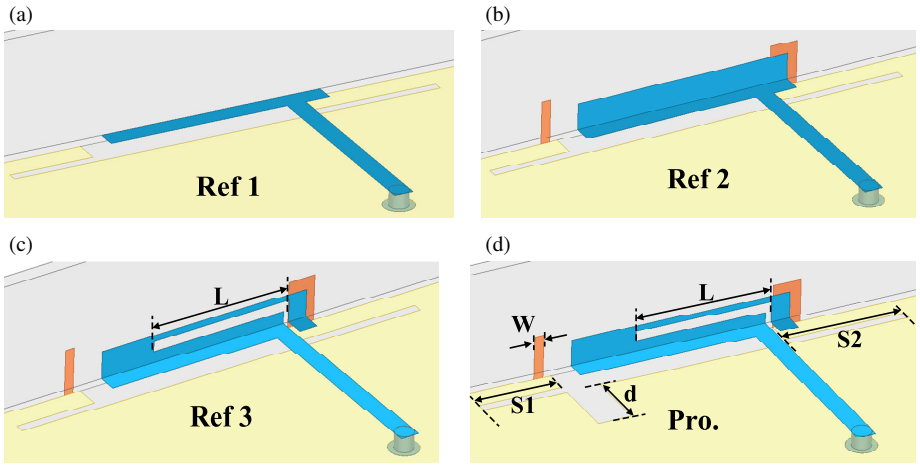

FIGURE 2. Antenna evolution of the suggested scheme. (a) Ref 1. (b) Ref 2. (c) Ref 3. (d) Proposed antenna element.

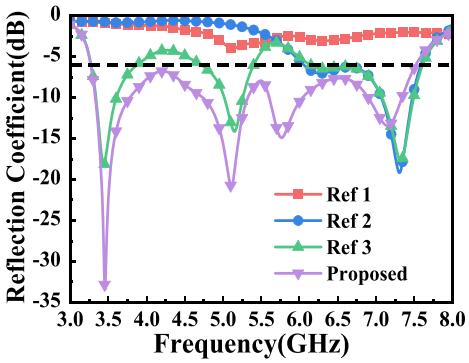

FIGURE 3. Comparison of reflection coefficients of the reference antenna elements and the proposed antenna elements.

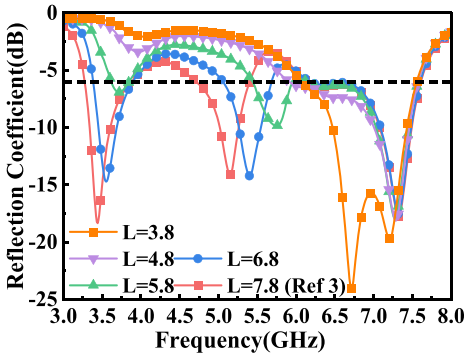

FIGURE 4. Reflection coefficients of antenna elements for different lengths of L in Ref 3 (Unit: mm).

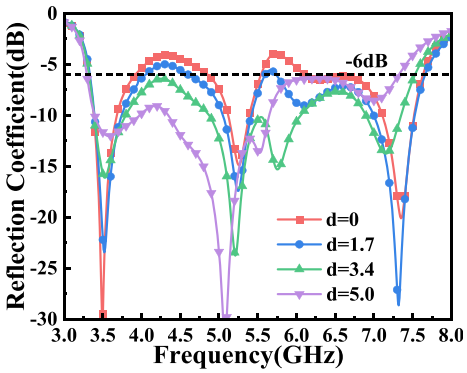

FIGURE 5. Reflection coefficients of antenna elements for different lengths of d in proposed antenna (Unit: mm).

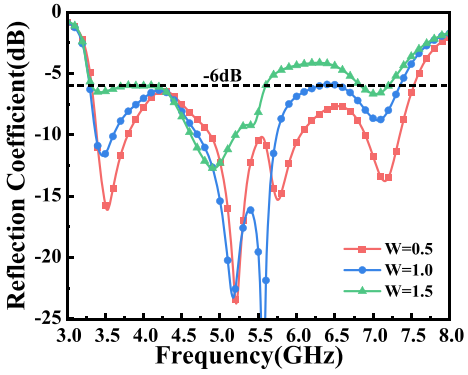

FIGURE 6. Reflection coefficients of antenna elements for different widths of W in proposed antenna (Unit: mm).

enhance the bandwidth, the feeder line was modified with L-slotting as described in [3]. Figure 4 shows the changes in the reflection coefficient due to adjustments in the horizontal length (L) of the slotted line, varying from 7.8 mm to 3.8 mm. The bandwidth gradually widens, and the low-frequency range is covered as the horizontal length L increases. In order to meet the performance requirement of wide bandwidth and coverage of 3.5 GHz band, the value of L is selected as 7.8 mm. This leads to a significant improvement in the performance of the antenna element. The blue curve in Figure 3, representing the reflection coefficient in [3], indicates three resonances in the 3–8 GHz range. However, [3] falls short in providing coverage for n79 and LTE band 46.

Further modifications were made to the grounded slot by adding a rectangular slot next to the T-slot, as shown in Figure 2(d), which represents the final model of the antenna construction. Figure 5 shows the effect of the length of the rectangular slot (denoted by d) on the antenna performance.

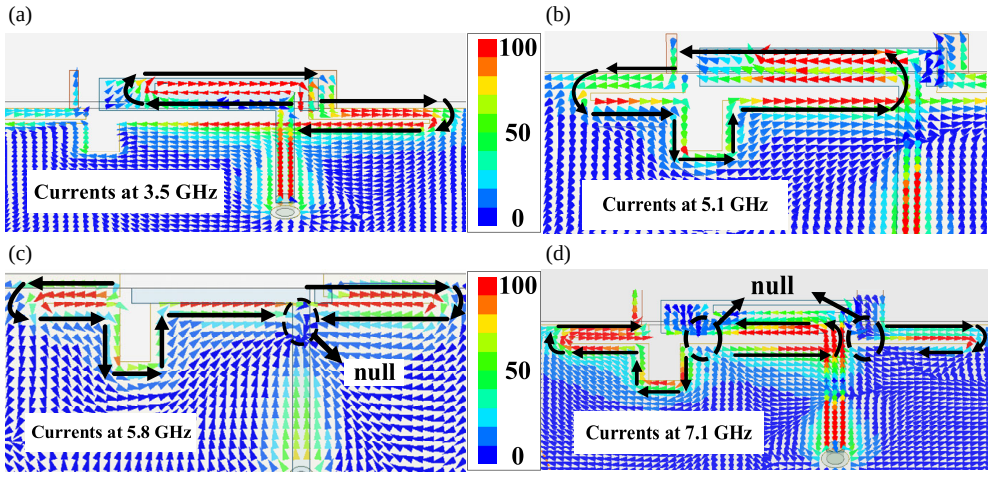

FIGURE 7. Simulated vector current distribution at four resonant frequencies. (a) 3.5 GHz, (b) 5.1 GHz, (c) 5.8 GHz, (d) 7.1 GHz.

The rectangular slot with a length of 3.4 mm has an exciting effect on the antenna performance, obtaining a wide bandwidth and good impedance matching, much better than the antenna performance of [3]. This modification shifts some of the resonance points of the antenna element from 4.5 GHz to 6 GHz towards lower frequencies, which greatly enhances the impedance matching.

In addition, the width of the left metal patch on the outer surface of the frame of the antenna unit has a significant effect on the antenna performance. Figure 6 depicts the reflection coefficients of the antenna when the width of the patch, W, is varied from 0.5 mm to 1.5 mm. The smaller patch size instead widens the bandwidth of the antenna, and W is finally optimized to 0.5 mm.

The above design, dependent on the modification of three elements in each antenna, results in a configuration that is superior in performance while not being overly complex and easy to work with. Each step of improvement to the design process results in enhanced antenna performance, and the proposed antenna has a large band coverage that can be well suited for 5G smartphone applications.

In Figure 7, the simulated vector current distributions at the four resonances are depicted to understand the mechanism of operation.

At the resonant frequency of 3.5 GHz, the currents are mainly distributed on the right side of the L-shaped feeder and the slots on the ground plane. The currents form a coupled loop current distribution around the tuning branch created by the slots on the microstrip feeder and the slots on the ground plane. This distribution is free of current nulls and is excited at a quarter wavelength. At the resonant frequency of 5.1 GHz, the current is distributed to the left of the slots in the feeder strip and in the ground plane, also excited at a quarter wavelength similar to the case of the resonance at 3.5 GHz. At the resonant frequency of 5.8 GHz, the antenna element is primarily excited by the slot mode, as depicted in Figure 7(c). Here, the current is distributed around the gun-shaped slot, with a current null in the middle, forming a half-wavelength slot mode structure. At the resonance frequency of 7.1 GHz, as shown in Figure 7(d), the current distribution has two current nulls, which divide the current loop formed by the microstrip line and the slot into three segments. All segments are excited by the half-wavelength mode, leading to the formation of the high-frequency partial resonance at 7.1 GHz.

2.3. Analysis of Antenna Parameters

As evident from the current analysis, all four resonant modes are influenced by the slots. This section delves into the impact of adjusting the slot sizes on the antenna's performance. We scanned and analyzed the effects of slot dimension variations, which include the length of narrow slots on either side of the ground plane slots ($S1$ and $S2$ — representing the left short and right long slot lengths, respectively, as shown in Figure 2(d)), to delve into its operational mechanisms

As depicted in Figure 8(a), the transmission coefficient varies as $S1$ increases from 3.5 mm to 6.5 mm. It is evident that the length of $S1$ minimally impacts the resonance at the 3.5 GHz frequency. With the gradual reduction of $S1$, the resonance frequencies other than 3.5 GHz (5.1 GHz, 5.8 GHz, and 7.1 GHz) shift towards higher frequencies. This observation confirms the accuracy of the working mechanism in the current vector analysis discussed in the previous section. At 3.5 GHz, the resonance is excited by the loop mode on the right side, and therefore it is not affected by changes in slot dimensions on the left side. In Figure 8(b), the transmission coefficient changes as $S2$ ranges from 2.5 to 6.5 mm. The low-frequency resonance (3.5 GHz) shifts to lower frequencies with increasing $S2$. When $S2$ is 4.5 mm, only one resonance exists in the middle-frequency band. As $S2$ increases to 6.5 mm, the resonance in the middle part splits into two segments. This phenomenon is likely attributed to the shorter length of $S2$, which can only stimulate the loop mode resonance on the left side of the slot. However, as the slot length increases, it is separated into loop mode and slot mode, resulting in the lower frequency resonance (5.1 GHz) being excited by the loop mode and the higher frequency resonance (5.8 GHz) being excited by the slot mode.

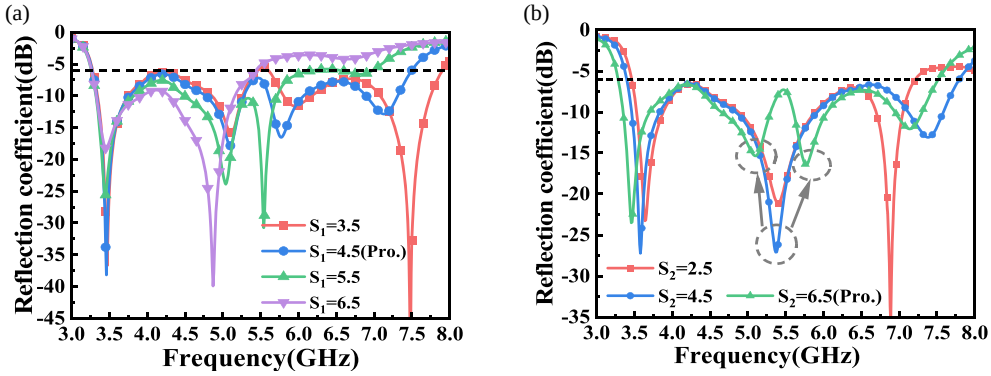

FIGURE 8. Effect on the simulated reflection coefficient of the antenna element when changing $S1$ and $S2$. (a) The value of $S1$ is adjusted. (b) The value of $S1$ is adjusted (Unit: mm).

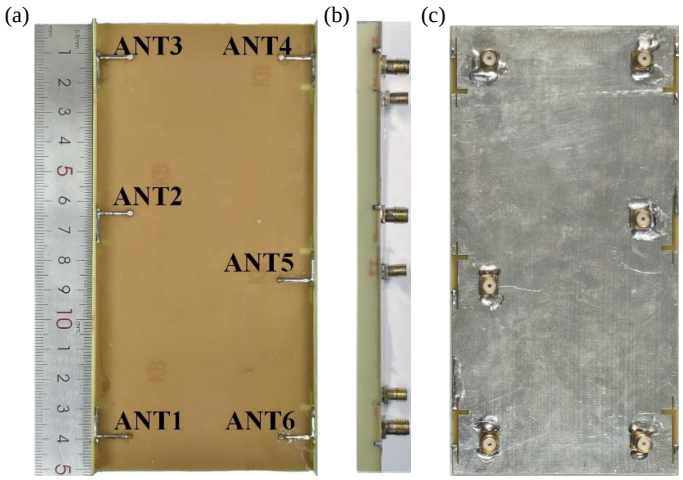

FIGURE 9. Photos of the measured MIMO array. (a) Overhead view. (b) Side frame view. (c) Back view.

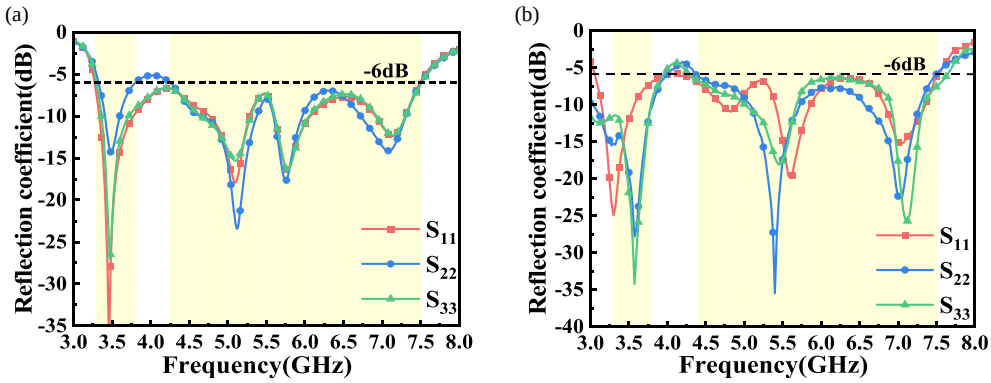

FIGURE 10. Simulated S-parameters versus measured S-parameters of the proposed MIMO array. (a) Simulated reflection coefficients of ANTs 1–3. (b) Measured reflection coefficients of ANTs 1–3.

3. RESULTS AND DISCUSSION

In order to verify the effectiveness of the antennas, a physical model of the proposed antenna array was fabricated and tested in the laboratory. The proposed antenna is designed using HFSS simulation software, and the printed circuit board (PCB) is fabricated based on the design model. The antennas are clad with copper, punched and etched on the main substrate and frame substrate made of Fr-4 material. Finally, the substrate and frame are connected, and the SMA connectors as well as the antenna units are soldered to obtain the finished product for antenna testing.

As shown in Figure 9, a fabricated prototype of a six-port MIMO antenna system is demonstrated with six SMA connec-

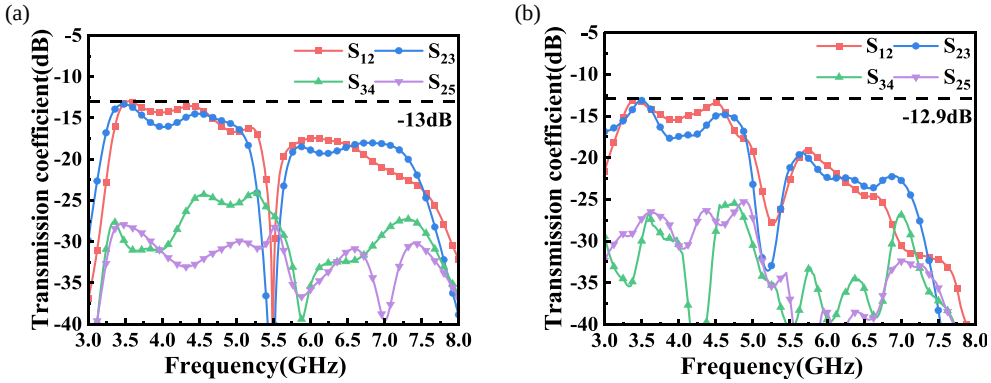

FIGURE 11. Transmission coefficients of the adjacent elements for the proposed MIMO array. (a) Simulated transmission coefficients. (b) Measured transmission coefficients.

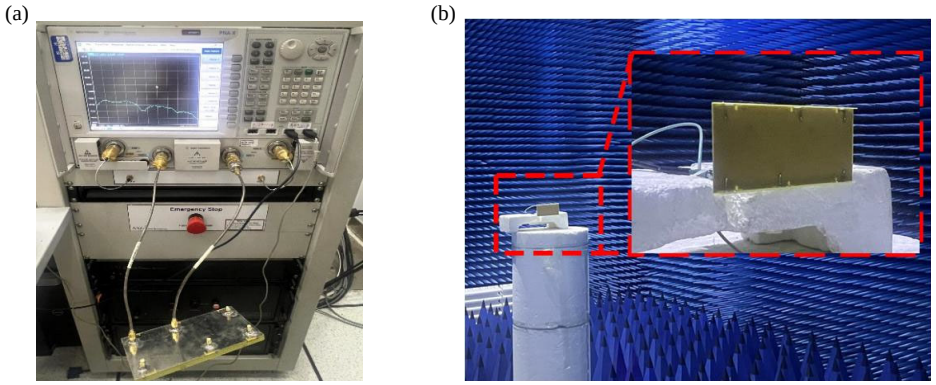

FIGURE 12. The environment of the antenna measurement. (a) Measurement of S-parameters. (b) Measurement environment for radiation direction.

tors under the metal ground feeding each of the six antenna elements.

3.1. S-Parameters and Antenna Efficiency

Due to the centrosymmetric structure of this MIMO antenna, simulations and measurements of reflection coefficients and efficiencies are provided for one side port only. The S-parameters of the antenna were measured using an N5247A PNA-X network analyzer. Figure 10 illustrates the simulated and measured values of the reflection coefficient. The simulated and measured results are similar, and the proposed MIMO antenna has -6 dB impedance bandwidths of 14.28% (3.3–3.8 GHz) and 52.10% (4.4–7.5 GHz) covering both n78/n79 and LTE Band 46. The isolation of the neighboring antenna elements is better than 12.9 dB, and the isolation of the relative antenna elements is better than 25 dB, as shown in Figure 11.

The measured environment is shown in Figure 12. Meanwhile, the values of the respective simulated antenna efficiencies of ANTs 1–3 are shown in Figure 13, achieving antenna efficiencies higher than 60% in the range of bands in which they operate.

3.2. Radiation Pattern and MIMO Performance

Due to the central symmetry of the antenna, for simplicity, the simulated and measured normalized radiations of the ANTs 1–3 in the XOZ and YOZ planes are plotted in Figures 14, 15, and 16 for each resonant frequency (3.5 GHz, 5.1 GHz, 5.8 GHz, and 7.1 GHz), respectively. The simulated and measured radiation direction plots are in good agreement, with the radiation in the XOZ plane indicated by the red curves mostly pointing towards the X-axis direction and with the effect particularly pronounced for ANT 1 and ANT 3, whereas the radiation in the YOZ plane indicated by the blue curves mostly points towards the Y-axis, and the main radiation direction of the antenna elements of each port is away from the system ground for

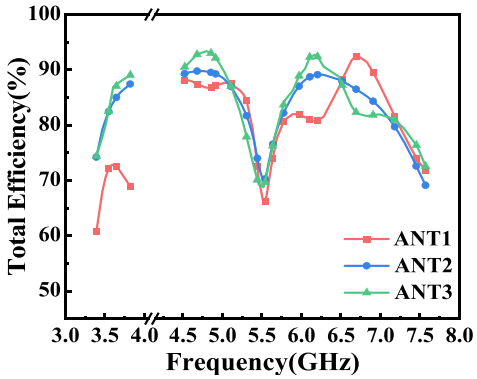

FIGURE 13. The total efficiency of ANT 1, ANT 2, and ANT 3 in the operating band.

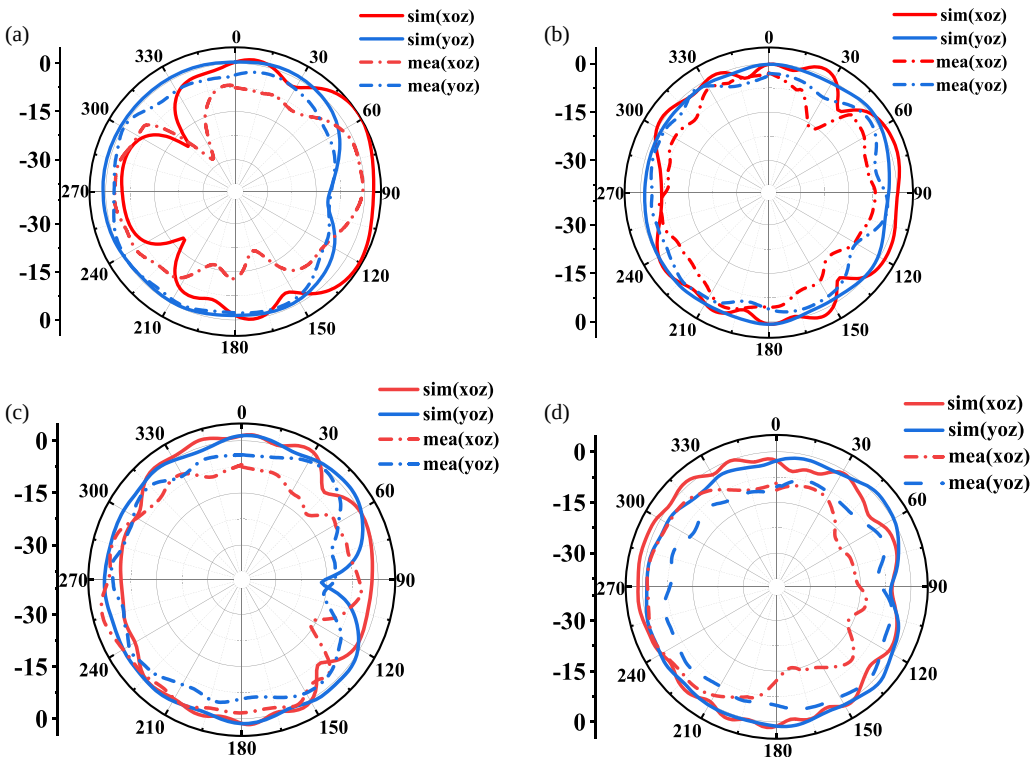

FIGURE 14. Normalized radiation patterns for ANT 1 simulations and measurements. (a) 3.5 GHz, (b) 5.1 GHz, (c) 5.8 GHz, (d) 7.1 GHz.

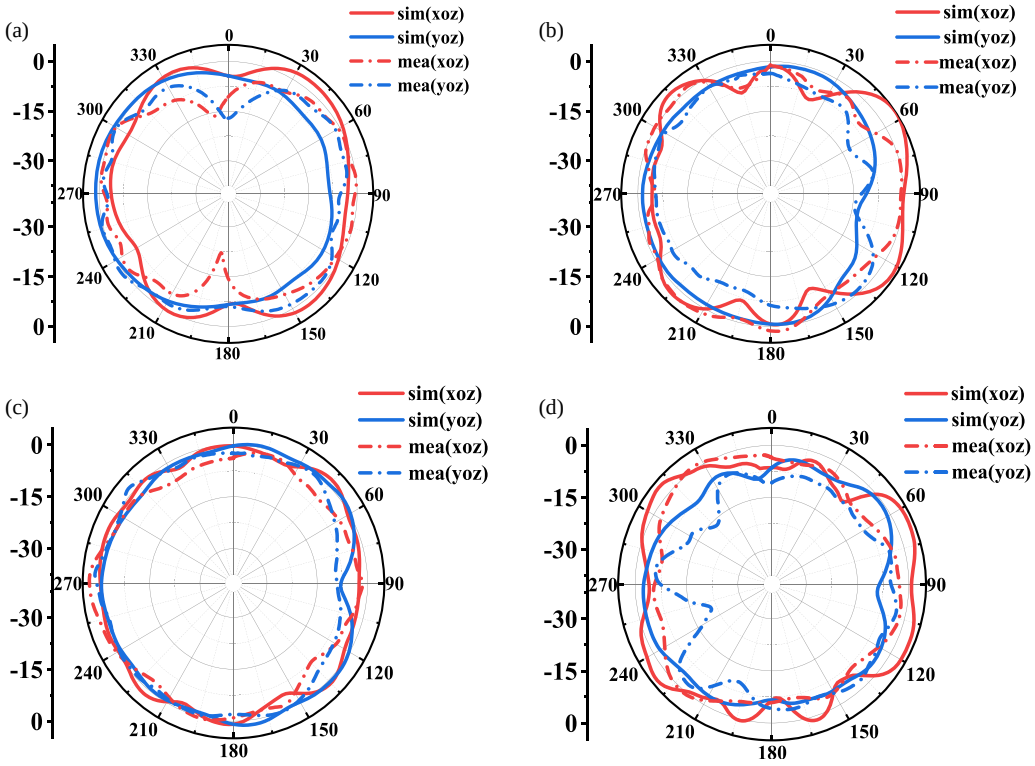

FIGURE 15. Normalized radiation patterns for ANT 2 simulations and measurements. (a) 3.5 GHz, (b) 5.1 GHz, (c) 5.8 GHz, (d) 7.1 GHz.

each resonance frequency. In summary, the antenna has good radiation omnidirectionality.

In addition, the Envelope Correlation Coefficient (ECC) is also given to evaluate the antenna performance. ECC is a time series representation of the relativity of the received signals be-

TABLE 1. Antenna performance comparison.

Ref.	Bandwidth (GHz)	Isolation (dB)	ECC	Total Efficiency (%)	Size ($L \times W \times H$ mm^3)
[3]	3.4–3.6(−6 dB)	> 16	< 0.05	59–73	$28.4 \times 1 \times 0.8$
[11]	3.4–3.6(−10 dB)	> 12.7	< 0.13	41–65	$25 \times 7 \times 1.5$
[14]	3.4–3.6(−10 dB)	> 19.1	< 0.0125	60–70	$17.4 \times 0.8 \times 6$
[16]	3.4–3.9, 4.5–5.3(−6 dB)	> 10	< 0.23	50–78	$7 \times 2.5 \times 6.2$
[22]	3.3–4.2, 4.4–5.0(−6 dB)	> 11	< 0.2	38–52	$11 \times 7 \times 5$
[24]	3.3–3.6, 4.4–5.85(−6 dB)	> 16.5	< 0.18	41.5–82.4	$7 \times 0.8 \times 6.8$
[28]	3.1–6.0(−6 dB)	> 10	< 0.1	41–69	$13.9 \times 0.8 \times 7$
[30]	3.3–7.5(−6 dB)	> 10	< 0.05	40–78	$15 \times 0.8 \times 7$
Pro.	3.3–3.8, 4.4–7.5(−6 dB)	> 12.9	< 0.18	60–93	$23 \times 5 \times 2.3$

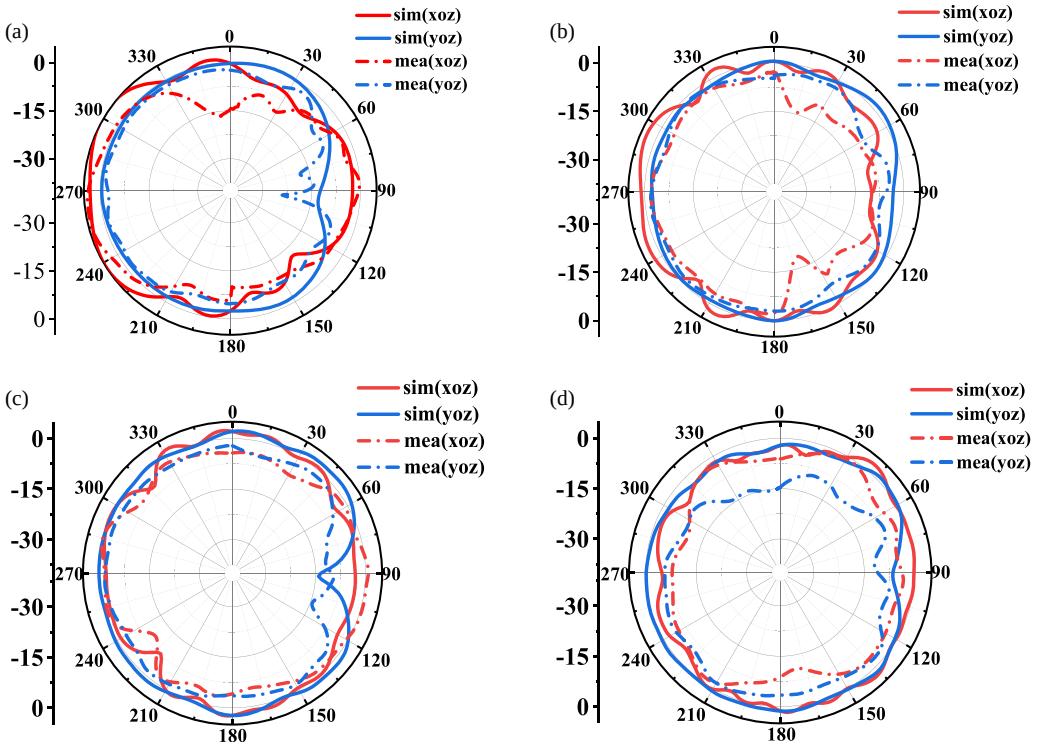

FIGURE 16. Normalized radiation patterns for ANT 3 simulations and measurements. (a) 3.5 GHz, (b) 5.1 GHz, (c) 5.8 GHz, (d) 7.1 GHz.

tween two antenna elements in an antenna system, and it is a very important metric for examining the diversity performance of a MIMO antenna system. According to Equation (1) of ECC [32], the result of ECC is derived from the measured S-parameters as shown in Figure 17. The results show that the ECC is less than 0.18 in all operating frequency bands, which is better than the operating standard of less than 0.5.

$$\mathrm{ECC} = \frac{\left|S_{12}^{*}S_{12} + S_{21}^{*}S_{22}\right|^{2}}{\left(1 - \left|S_{11}\right|^{2} - \left|S_{21}\right|^{2}\right)\left(1 - \left|S_{22}\right|^{2} - \left|S_{12}\right|^{2}\right)} \quad (1)$$

3.3. Comparison with Existing 5G Smartphone Antennas

In order to demonstrate the superiority of the antenna designed in this paper, the previously reported MIMO smartphone antennas are compared. In Table 1, the various performances of each antenna are demonstrated. Although the antenna designs in [3] and [14] have high isolation up to 19.1, they only cover a single frequency band and cannot be used for multi-band application scenarios. Both [16] and [22] cover n78 and n79 bands but lack LTE band 46 and have slightly poorer isolation than the proposed antenna. The antenna design in [30] relies on its antenna height of 7 mm to operate from 3.3 to 7.5 GHz. However, the proposed antenna has a height of only 2.3 mm and still satisfies most of the bands, and its isolation degree of 12.9 dB is better than the 10 dB isolation degree of [30]. The proposed an-

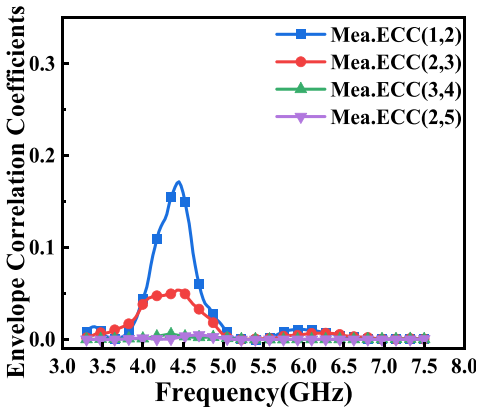

FIGURE 17. Calculated envelope correlation coefficient values from the measured results.

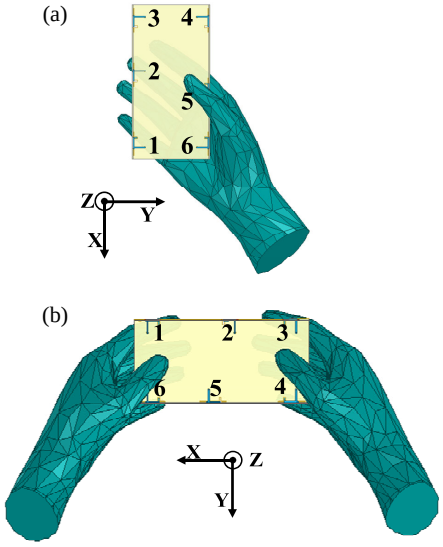

FIGURE 18. Two typical usage scenarios under user's hand operation. (a) SHO mode. (b) DHO mode.

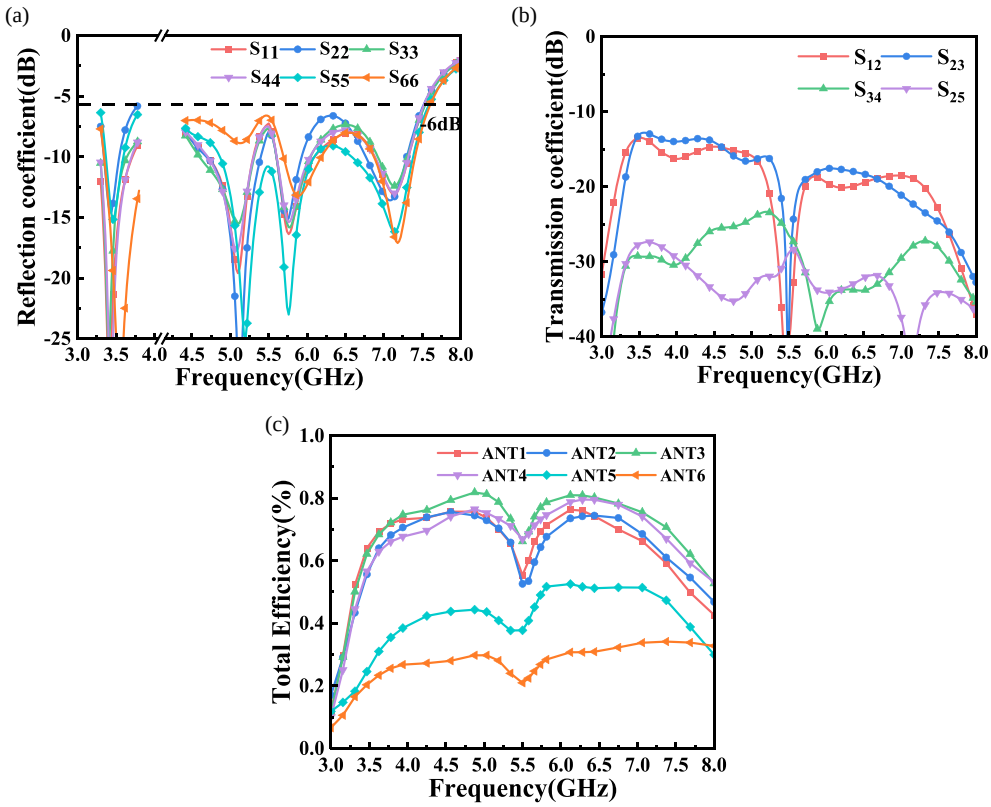

FIGURE 19. Simulated parameters under SHO. (a) Reflection coefficient. (b) Transmission coefficient. (c) Total efficient.

tenna in this paper has the advantages of wide bandwidth, small size, and better isolation than these designs in the literature.

4. EFFECT OF USER'S HAND

To further explore the operational performance of the antenna in realistic scenarios, the influence of the user's hand is investigated in this section. Two typical 5G usage scenarios, namely, single-hand operation mode (SHO) and dual-hand operation mode (DHO), are depicted in Figure 18.

As shown in Figure 19, the reflection coefficient, transmission coefficient, and radiation efficiency of each antenna port are shown for the antenna in SHO mode. Figure 19(a) shows that the reflection coefficient of ANT 6 is significantly weakened, which is due to the direct contact of the hand type on ANT 6, making it the most affected; its return loss has a slight

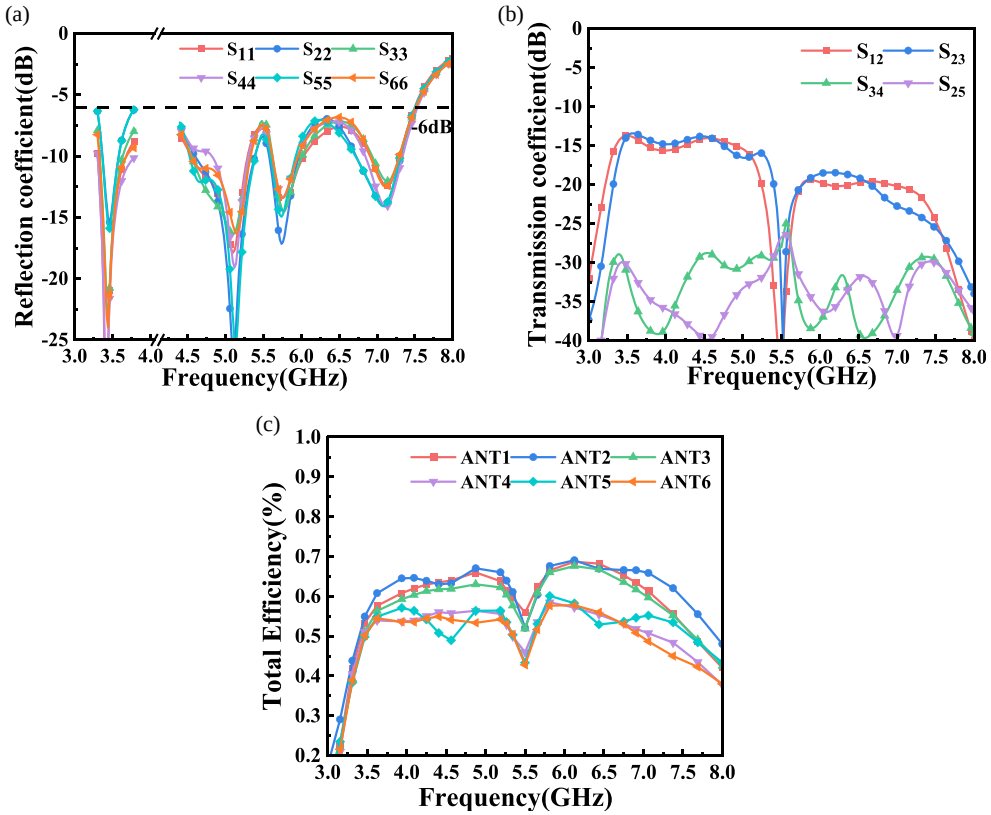

FIGURE 20. Simulated parameters under DHO. (a) Reflection coefficient. (b) Transmission coefficient. (c) Total efficient.

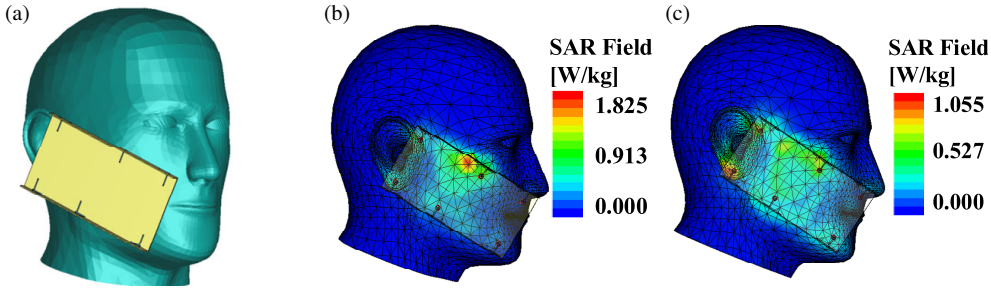

FIGURE 21. Simulated 1-g-spatial-average Head SAR. (a) The simulated environment. Head SAR-Field at (b) 3.5 GHz and (c) 6.0 GHz.

increase, but still maintains the original operating band; the rest of the components are not in direct contact; the reflection coefficient is almost unaffected. From Figure 19(b), the isolation between ports is still maintained at about 13 dB. From Figure 19(c), it can be seen that the radiation efficiency of ANT 6 and ANT 5, which are covered by the hand to the largest extent, decreases to less than 50%, while the efficiency of the rest of the antenna elements is still maintained at more than 50%.

The reflection coefficient, transmission coefficient, and radiation efficiency of each antenna port in the DHO mode are shown in Figure 20. The ports are distributed on the two long side edges of the frame, while DHO mode covers the two short edges and does not directly cover the antenna. As a result, the reflection coefficients of the ports are not greatly affected and remain in their original operating bands, as shown in Figure 20(a). The isolation is not affected as shown in Figure 20(b). Figure 20(c) shows that the radiation efficiency of each antenna element is weakened to different degrees, and ANTs 1–3 near the index finger are more efficient, which are all between 50% and 70%. However, the efficiency of ANTs 4–6 near the palm drops from 40% to 60%.

5. SAR ANALYSIS

Specific Absorption Rate (SAR) is used to describe the effect of electromagnetic radiation on the human body. The European standard [33] states that the maximum value of any 1-g-spatial-average head SAR for mobile phone antennas should not exceed 2 W/kg. 1-g-spatial-average head SAR of the proposed antenna is simulated at the respective central frequencies of the two frequency bands (3.5 GHz and 6 GHz) as shown in Figure 21. The simulation environment is shown in Figure 21(a), and the simulation is strictly based on the Cellular Telecommunications Industry Association (CTIA) test plan [34] with an

input power of 23 dBm. The SAR-Field at the two frequencies is shown in Figures 21(b), (c), and it can be seen that the simulated head SAR maxima at 3.5 GHz and 6 GHz are 1.825 W/kg and 1.055 W/kg, respectively, which are compliant with the European standard.

All the above simulation results were obtained using the HFSS 19.2 version except for the SAR analysis. The SAR analyses were performed using CST Studio Suite version 2024.

6. CONCLUSION

A six-port dual-band antenna with high isolation for 5G smartphone applications is proposed in this paper. The broadband characteristics are achieved through the combination of two coupled feed loop mode resonances (3.5 GHz and 5.1 GHz) and two slot mode resonances (5.8 GHz and 7.1 GHz). The proposed antenna covers both ends of the operating band, ranging from 3.3–3.8 GHz to 4.4–7.5 GHz, encompassing both n78/n79 and LTE band 46. The proposed antenna system is characterized by suppressed mutual coupling (< 12.9 dB), high overall antenna efficiency (60–93%), and good MIMO performance (ECC < 0.18). The simulated and measured results of this new antenna are consistent and perform well enough to be used in real-world production, providing a new option for 5G smartphone antennas. The ECC value in handheld mode is less affected, and the antenna's head SAR value complies with EU standards, combining stability and safety. However, the choice of materials and the integration of various antennas inside the phone still pose challenges to the commercialization of this antenna promising subsequent in-depth research. In conclusion, the proposed antenna demonstrates superior performance and is better suited to meet the requirements of future 5G smartphone application development.

ACKNOWLEDGEMENT

This work was supported in part the Natural Science Research Project of Anhui Educational Committee under No. 2022AH051583, in part by the Anhui Province Graduate Academic Innovation Project under grant No. 2023xscx074.

REFERENCES

[1] Shafi, M., A. F. Molisch, P. J. Smith, T. Haustein, P. Zhu, P. D. Silva, F. Tufvesson, A. Benjebbour, and G. Wunder, "5G: A tutorial overview of standards, trials, challenges, deployment, and practice," *IEEE Journal on Selected Areas in Communications*, Vol. 35, No. 6, 1201–1221, 2017.

[2] Jensen, M. A. and J. W. Wallace, "A review of antennas and propagation for MIMO wireless communications," *IEEE Transactions on Antennas and Propagation*, Vol. 52, No. 11, 2810–2824, 2004.

[3] Ren, A., Y. Liu, and C.-Y.-D. Sim, "A compact building block with two shared-aperture antennas for eight-antenna MIMO array in metal-rimmed smartphone," *IEEE Transactions on Antennas and Propagation*, Vol. 67, No. 10, 6430–6438, 2019.

[4] Jiang, W., Y. Cui, B. Liu, W. Hu, and Y. Xi, "A dual-band MIMO antenna with enhanced isolation for 5G smartphone applications," *IEEE Access*, Vol. 7, 112 554–112 563, 2019.

[5] Ren, A., Y. Liu, H.-W. Yu, Y. Jia, C.-Y.-D. Sim, and Y. Xu, "A high-isolation building block using stable current nulls for 5G smartphone applications," *IEEE Access*, Vol. 7, 170 419–170 429, 2019.

[6] Liu, D. Q., H. J. Luo, M. Zhang, H. L. Wen, B. Wang, and J. Wang, "An extremely low-profile wideband MIMO antenna for 5G smartphones," *IEEE Transactions on Antennas and Propagation*, Vol. 67, No. 9, 5772–5780, 2019.

[7] Zou, H., Y. Li, B. Xu, Y. Chen, H. Jin, G. Yang, and Y. Luo, "Dual-functional MIMO antenna array with high isolation for 5G/WLAN applications in smartphones," *IEEE Access*, Vol. 7, 167 470–167 480, 2019.

[8] Parchin, N. O., Y. I. A. Al-Yasir, A. H. Ali, I. Elfergani, J. M. Noras, J. Rodriguez, and R. A. Abd-Alhameed, "Eight-element dual-polarized MIMO slot antenna system for 5G smartphone applications," *IEEE Access*, Vol. 7, 15 612–15 622, 2019.

[9] Liu, Y., A. Ren, H. Liu, H. Wang, and C.-Y.-D. Sim, "Eight-port MIMO array using characteristic mode theory for 5G smartphone applications," *IEEE Access*, Vol. 7, 45 679–45 692, 2019.

[10] Li, Y., C.-Y.-D. Sim, Y. Luo, and G. Yang, "High-isolation 3.5 GHz eight-antenna MIMO array using balanced open-slot antenna element for 5G smartphones," *IEEE Transactions on Antennas and Propagation*, Vol. 67, No. 6, 3820–3830, 2019.

[11] Chang, L., Y. Yu, K. Wei, and H. Wang, "Polarization-orthogonal co-frequency dual antenna pair suitable for 5G MIMO smartphone with metallic bezels," *IEEE Transactions on Antennas and Propagation*, Vol. 67, No. 8, 5212–5220, 2019.

[12] Chen, Q., H. Lin, J. Wang, L. Ge, Y. Li, T. Pei, and C.-Y.-D. Sim, "Single ring slot-based antennas for metal-rimmed 4G/5G smartphones," *IEEE Transactions on Antennas and Propagation*, Vol. 67, No. 3, 1476–1487, 2019.

[13] Alja'afreh, S. S., B. Altarawneh, M. H. Alshamaileh, E. R. Almajali, R. Hussain, M. S. Sharawi, L. Xing, and Q. Xu, "Ten antenna array using a small footprint capacitive-coupled-shorted loop antenna for 3.5 GHz 5G smartphone applications," *IEEE Access*, Vol. 9, 33 796–33 810, 2021.

[14] Zhao, A. and Z. Ren, "Size reduction of self-isolated MIMO antenna system for 5G mobile phone applications," *IEEE Antennas and Wireless Propagation Letters*, Vol. 18, No. 1, 152–156, 2019.

[15] Hu, W., L. Qian, S. Gao, L.-H. Wen, Q. Luo, H. Xu, X. Liu, Y. Liu, and W. Wang, "Dual-band eight-element MIMO array using multi-slot decoupling technique for 5G terminals," *IEEE Access*, Vol. 7, 153 910–153 920, 2019.

[16] Chen, Z., Y. Liu, T. Yuan, and H. Wong, "A miniaturized MIMO antenna with dual-band for 5G smartphone application," *IEEE Open Journal of Antennas and Propagation*, Vol. 4, 111–117, 2023.

[17] Cui, L., J. Guo, Y. Liu, and C.-Y.-D. Sim, "An 8-element dual-band MIMO antenna with decoupling stub for 5G smartphone applications," *IEEE Antennas and Wireless Propagation Letters*, Vol. 18, No. 10, 2095–2099, 2019.

[18] Dong, J., S. Wang, and J. Mo, "Design of a twelve-port MIMO antenna system for multi-mode 4G/5G smartphone applications based on characteristic mode analysis," *IEEE Access*, Vol. 8, 90 751–90 759, 2020.

[19] Hu, W., Q. Li, H. Wu, Z. Chen, L. Wen, W. Jiang, and S. Gao, "Dual-band antenna pair with high isolation using multiple orthogonal modes for 5G smartphones," *IEEE Transactions on Antennas and Propagation*, Vol. 71, No. 2, 1949–1954, 2023.

[20] Chang, L., G. Zhang, and H. Wang, "Dual-band antenna pair with lumped filters for 5G MIMO terminals," *IEEE Transactions on Antennas and Propagation*, Vol. 69, No. 9, 5413–5423, 2021.

[21] Hu, W., L. Qian, S. Gao, L.-H. Wen, Q. Luo, H. Xu, X. Liu, Y. Liu, and W. Wang, "Dual-band eight-element MIMO array using multi-slot decoupling technique for 5G terminals," *IEEE Access*, Vol. 7, 153 910–153 920, 2019.

[22] Ahn, J., Y. Youn, B. Kim, J. Lee, N. Choi, Y. Lee, G. Kim, and W. Hong, "Wideband 5G N77/N79 4×4 MIMO antenna featuring open and closed stubs for metal-rimmed smartphones with four slits," *IEEE Antennas and Wireless Propagation Letters*, Vol. 22, No. 12, 2798–2802, 2023.

[23] Chen, H.-D., Y.-C. Tsai, C.-Y.-D. Sim, and C. Kuo, "Broadband eight-antenna array design for sub-6 GHz 5G NR bands metal-frame smartphone applications," *IEEE Antennas and Wireless Propagation Letters*, Vol. 19, No. 7, 1078–1082, 2020.

[24] Li, H., S. Xiao, L. He, Q. Cai, and G. Liu, "A dual-band 8-antenna array design for 5G/WiFi 5 metal-frame smartphone applications," *Micromachines*, Vol. 15, No. 5, 584, 2024.

[25] Pandya, K., T. Upadhyaya, U. Patel, V. Sorathiya, A. Pandya, A. J. A. Al-Gburi, and M. M. Ismail, "Performance analysis of quad-port UWB MIMO antenna system for sub-6 GHz 5G, WLAN and X band communications," *Results in Engineering*, Vol. 22, 102318, 2024.

[26] Sun, L., Y. Li, and Z. Zhang, "Wideband integrated quad-element MIMO antennas based on complementary antenna pairs for 5G smartphones," *IEEE Transactions on Antennas and Propagation*, Vol. 69, No. 8, 4466–4474, 2021.

[27] Cai, Q., Y. Li, X. Zhang, and W. Shen, "Wideband MIMO antenna array covering 3.3–7.1 GHz for 5G metal-rimmed smartphone applications," *IEEE Access*, Vol. 7, 142 070–142 084, 2019.

[28] Sim, C.-Y.-D., H.-Y. Liu, and C.-J. Huang, "Wideband MIMO antenna array design for future mobile devices operating in the 5G NR frequency bands n77/n78/n79 and LTE band 46," *IEEE Antennas and Wireless Propagation Letters*, Vol. 19, No. 1, 74–78, 2020.

[29] Varheenmaa, H., P. Ylä-Oijala, A. Lehtovuori, and V. Viikari, "Wideband sub-6 GHz MIMO antenna for full-screen metal rim smartphones," *IEEE Access*, Vol. 11, 111 888–111 896, 2023.

[30] Yuan, X.-T., Z. Chen, T. Gu, and T. Yuan, "A wideband PIFA-pair-based MIMO antenna for 5G smartphones," *IEEE Antennas and Wireless Propagation Letters*, Vol. 20, No. 3, 371–375, 2021.

[31] Al-Gburi, A. J. A., N. H. M. Radi, T. Saeidi, N. J. Mohammed, Z. Zakaria, G. S. Das, A. Buragohain, and M. M. Ismail, "Superconductive and flexible antenna based on a tri-nanocomposite of graphene nanoplatelets, silver, and copper for wearable electronic devices," *Journal of Science: Advanced Materials and Devices*, Vol. 9, No. 3, 100773, 2024.

[32] Hallbjorner, P., "The significance of radiation efficiencies when using S-parameters to calculate the received signal correlation from two antennas," *IEEE Antennas and Wireless Propagation Letters*, Vol. 4, 97–99, 2005.

[33] Repacholi, M. H., M. Grandolfo, A. Ahlbom, U. Bergqvist, J. H. Bernhardt, J. P. Césarini, A. F. McKinlay, D. H. Sliney, *et al.*, "Health issues related to the use of hand-held radiotelephones and base transmitters," *Health Physics*, Vol. 70, No. 4, 587–593, 1996.

[34] CTIA, "The wireless association," Certification Test Plans, [Online]. Available: https://www.ctia.org/about-ctia/test-plans/.